

Band Versus Polaron: Charge Transport in Antimony Chalcogenides

Xinwei Wang,[†] Alex M. Ganose,[†] Seán R. Kavanagh,^{†,‡} and Aron Walsh^{*,†}

[†] *Department of Materials, Imperial College London, Exhibition Road, London SW7 2AZ, UK*

[‡] *Thomas Young Centre and Department of Chemistry, University College London, 20 Gordon Street, London WC1H 0AJ, UK*

E-mail: a.walsh@imperial.ac.uk

Abstract

Antimony sulfide (Sb_2S_3) and selenide (Sb_2Se_3) are emerging earth-abundant absorbers for photovoltaic applications. Solar cell performance depends strongly on charge carrier transport properties, but these remain poorly understood in Sb_2X_3 ($\text{X} = \text{S}, \text{Se}$). Here we report band-like transport in Sb_2X_3 by investigating the electron-lattice interaction and theoretical limits of carrier mobility using first-principles density functional theory and Boltzmann transport calculations. We demonstrate that transport in Sb_2X_3 is governed by large polarons with moderate Fröhlich coupling constants ($\alpha \approx 2$), large polaron radii (extending over several unit cells) and high carrier mobility (an isotropic average of $>10 \text{ cm}^2 \text{ V}^{-1} \text{ s}^{-1}$ for both electrons and holes). The room temperature mobility is intrinsically limited by scattering from polar phonon modes and is further reduced in highly defective samples. Our study confirms that the performance of Sb_2X_3 solar cells is not limited by intrinsic self-trapping.

Antimony chalcogenides (Sb_2X_3 ; $\text{X}=\text{S}, \text{Se}$) have emerged as promising light absorbing materials due to their attractive electronic and optical properties, including ideal band gaps

(1.1–1.8 eV) and high optical absorption coefficients ($>10^5 \text{ cm}^{-1}$).^{1–11} They are binary compounds with earth-abundant, low-cost and non-toxic constituents. The power conversion efficiencies (PCEs) in Sb_2X_3 solar cells have improved rapidly over the past decade, with record efficiencies reaching 7.50 % and 10.12 % for Sb_2S_3 and Sb_2Se_3 , respectively.^{12,13} Nevertheless, efficiencies are still well below those seen in state-of-the-art CdTe or hybrid halide perovskite devices, which have reached above 25 % under laboratory conditions.¹⁴

The underlying efficiency bottleneck is unclear. While the structural, electronic and optical properties of Sb_2X_3 have been widely investigated, the charge carrier dynamics, which critically affect conversion efficiencies, remain controversial. Charge carrier transport in Sb_2X_3 has been reported by several studies,^{15–19} but there are several fundamental questions that remain unanswered. The first is whether the nature of carrier transport is band-like or thermally-activated hopping. Yang et al.¹⁵ studied the charge carrier dynamics in Sb_2S_3 and ascribed the observed 0.6 eV Stokes shift to self-trapped excitons, suggesting hopping transport. In contrast, Liu et al.²⁰ and Zhang et al.¹⁷ argued against self-trapping in Sb_2Se_3 due to the saturation of fast signal decay with increasing carrier density. Considering it is challenging for direct measurements to distinguish whether the photoexcited carriers are intrinsically self-trapped or trapped at defect sites,²¹ a systematic theoretical study on the carrier transport in Sb_2X_3 is necessary. The second issue is about the resulting charge carrier mobility. Measured mobilities in Sb_2X_3 show a large variation,^{2,19,22–26} in part due to different synthesis and characterisation methods. As such, the intrinsic limits to mobility in Sb_2X_3 are unclear and the scattering physics underlying transport is not yet understood.

In this work, we studied the tendency for polaron trapping and its effect on charge carrier transport in Sb_2X_3 by first-principles density functional theory (DFT) and Boltzmann transport calculations. The electron-lattice interaction in Sb_2X_3 was explored through the Fröhlich polaron coupling constant and Schultz polaron radius. Modelling of electron and hole polarons in Sb_2X_3 indicates the intrinsic formation of large polarons and contrast to recent suggestions of small polarons (i.e. self-trapped carriers).^{15,16} The prediction of large

polaron formation is further reinforced by the results of carrier transport calculations. The isotropically averaged mobilities are higher than $10 \text{ cm}^2 \text{ V}^{-1} \text{ s}^{-1}$ at room temperature and decrease with increasing temperature for both electrons and holes, further confirming the band-like transport in Sb_2X_3 . We find the intrinsic mobility is limited by scattering from polar optical phonons at low and moderate defect concentrations, while at high charged defect concentrations ($>10^{18} \text{ cm}^{-3}$) impurity scattering dominates. We expect our results will enable the design of Sb_2X_3 devices with improved efficiencies.

Sb_2X_3 crystallise in the orthorhombic $Pnma$ space group and are comprised of strongly bonded quasi-one-dimensional (1D) $[\text{Sb}_4\text{X}_6]_n$ ribbons oriented along the $[100]$ direction (Fig. 1). Ribbon formation is driven by the Sb lone pair with ribbons stacked together by weak interactions.¹¹ According to our previous optimization using the HSE06 hybrid functional and D3 dispersion correction,¹¹ the calculated lattice parameters are 3.80/3.95 Å, 11.20/11.55 Å and 11.39/11.93 Å for $\text{Sb}_2\text{S}_3/\text{Sb}_2\text{Se}_3$ along the a , b and c axes, respectively. Sb_2X_3 are indirect band gap semiconductors with calculated indirect/direct band gaps of 1.79/1.95 eV and 1.42/1.48 eV for Sb_2S_3 and Sb_2Se_3 , respectively, which are in reasonable agreement with previous experimental^{1–5,27–29} and theoretical studies.^{6–9,30} The electronic band structures are shown in Fig. S1 of the Supplementary Information. It has been widely suggested that efficient transport can only happen along the ribbons, based on the understanding that Sb_2X_3 are 1D semiconductors.^{31–35} However, neither the structural dimensionality nor the electronic dimensionality of Sb_2X_3 is 1D.^{11,36}

Charge carriers in crystals are formally described as quasi-particles due to their interaction with the extended structure. In polar semiconductors, the charge carriers and the surrounding lattice deformation form a so-called polaron,³⁷ which determines the nature of carrier transport. Polarons can be classified into two types based on the strength of electron-phonon coupling. Stronger coupling leads to larger local lattice distortion which provides the driving force for small polarons to form. Thus, for a small polaron, the lattice deformation is usually confined to one unit cell, and a carrier's motion is typically incoherent with thermally

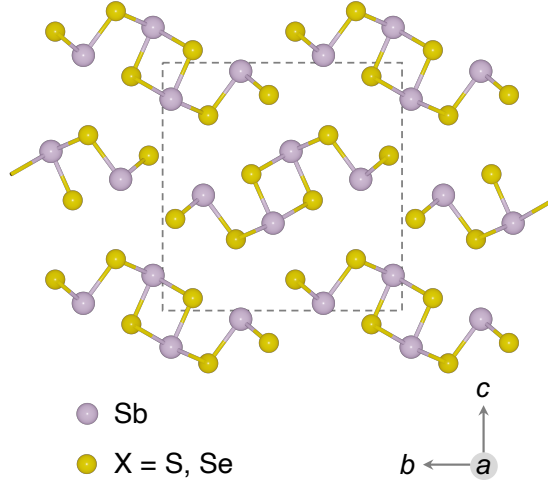


Figure 1: Ground-state crystal structure ($Pnma$ space group) of Sb_2X_3 . The conventional unit cell is represented by a rectangle.

Table 1: Calculated Fröhlich parameter (α) and Schultz polaron radius (r_f) for electrons (e^-) and holes (h^+) in Sb_2S_3 and Sb_2Se_3 at $T = 300$ K

Material		α		r_f (Å)	
		e^-	h^+	e^-	h^+
Sb_2S_3	avg	1.6	2.0	45.5	40.4
	x	1.0	1.8	57.3	43.7
	y	2.4	2.1	36.9	40.3
	z	5.7	2.5	23.7	36.4
Sb_2Se_3	avg	1.3	2.1	40.5	31.9
	x	0.8	2.0	50.9	32.4
	y	2.0	1.6	32.8	36.1
	z	5.8	3.8	18.8	23.5

activated hops which lead to low mobility ($\ll 1 \text{ cm}^2 \text{ V}^{-1} \text{ s}^{-1}$). By contrast, the lattice deformation in a large polaron is usually moderate and spreads over multiple unit cells, resulting in a higher mobility ($> 1 \text{ cm}^2 \text{ V}^{-1} \text{ s}^{-1}$). In polar crystals, the electron-phonon interaction is usually dominated by the coupling of charge carriers to the longitudinal optical (LO) phonons, which can be described within the Fröhlich model.³⁸

We first evaluate the Fröhlich interaction by the coupling constant α . The calculated α (shown in Table 1) shows an isotropically averaged value of ~ 2 for both Sb_2S_3 and Sb_2Se_3 , which falls in the intermediate electron-phonon coupling regime (defined as $0.5 \lesssim \alpha \lesssim 6$).³⁹

The magnitude of α along the [100] and [010] directions is quite close ($\Delta\alpha = 1.2$ – 1.4 and 0.3 – 0.4 for electrons and holes, respectively), suggesting similar electron-phonon interaction strengths along these two directions. We further estimate the size of polarons in Sb_2X_3 by the Schultz polaron radius (r_f).⁴⁰ The large values of electron and hole polaron radii (which extend over multiple structural units) indicate the polarons are delocalised in both Sb_2S_3 and Sb_2Se_3 . The details of parameters used and the procedure for averaging α can be found in Section S2 of the Supplementary Information.

For an alternative assessment, we performed direct first-principles DFT calculations to model charge carriers in Sb_2X_3 . There are two challenges for reliable polaron modelling. The first is the self-interaction error⁴¹ arising from the approximate form of the exchange-correlation functional which causes electrons to spuriously delocalise.^{42,43} This is typically resolved by employing a hybrid functional^{44–46} which incorporates a certain amount of exact Fock exchange or by a Hubbard correction (DFT+U).^{47,48} Secondly, the formation of localised polarons is dependent on the initial geometries and wavefunctions. Different methods have been proposed to break the crystal symmetry and promote the formation of localised states. Among them, the bond distortion method and electron attractor method have proved reliable across a range of structures and chemistries.^{21,43,49–53} The former involves introducing local perturbations in a supercell in a region where the polaron is expected to localise, while the latter uses a temporarily-substituted atom to attract an electron or a hole, which is then removed and the structure re-relaxes. In this work, all polaron calculations were performed using the HSE06 hybrid exchange-correlation functional. We attempted to localise electron and hole polarons by adding or removing an electron from a Sb_2X_3 supercell using both these distortion methods. The full computational details and workflow are provided in Section S4 (Fig. S3). No energy lowering distortions were found in any case. The electrons and holes always preferred to delocalise rather than localise in both Sb_2S_3 and Sb_2Se_3 (see Fig. S4 and S5), indicating again that small polarons are unlikely to form intrinsically by self-trapping. This is also supported by recent experimental evidence that the trap states in

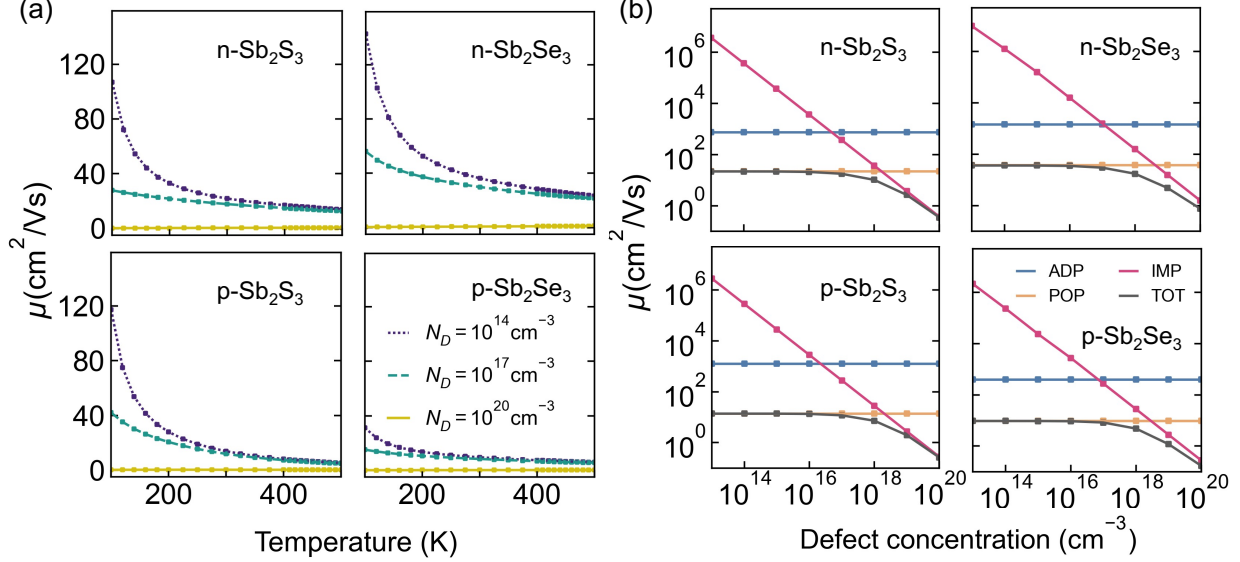


Figure 2: (a) Calculated average mobilities of electrons and holes in Sb_2S_3 and Sb_2Se_3 as a function of temperature with different defect concentrations. (b) Calculated total and component mobilities as a function of bulk defect concentration at 300 K. ADP, acoustic deformation potential; POP, polar optical phonon; IMP, ionized impurity. N_D , defect concentration.

Sb_2Se_3 are saturated by moderate density photocarriers.²⁰

As self-trapping could originate from either self-trapped carriers (i.e. small polarons) or self-trapped excitons, we next consider the possibility of forming self-trapped excitons. Firstly, the large dielectric constants (~ 100) and small effective masses (~ 0.1) in Sb_2X_3 ¹¹ suggest that the Coulomb interaction is strongly screened and a large exciton radius is favoured. The small experimental exciton binding energies (0.01–0.05 eV for Sb_2S_3 and 0.04 eV for Sb_2Se_3)^{31,54} further indicate weak electron-hole interactions in Sb_2X_3 . Additionally, experimental measurements of the imaginary part of the frequency-dependent complex photoconductivity in Sb_2Se_3 do not reveal any negative components⁵⁵ that can be a signal of exciton formation. Consequently, we conclude that self-trapped excitons in Sb_2X_3 are unlikely.

To further understand the nature of transport in Sb_2X_3 the first-principles carrier mobility⁵⁷ was calculated. Both n -type and p -type doping were investigated, with calculations including scattering from ionized impurities (IMP), acoustic phonons (ADP) and polar opti-

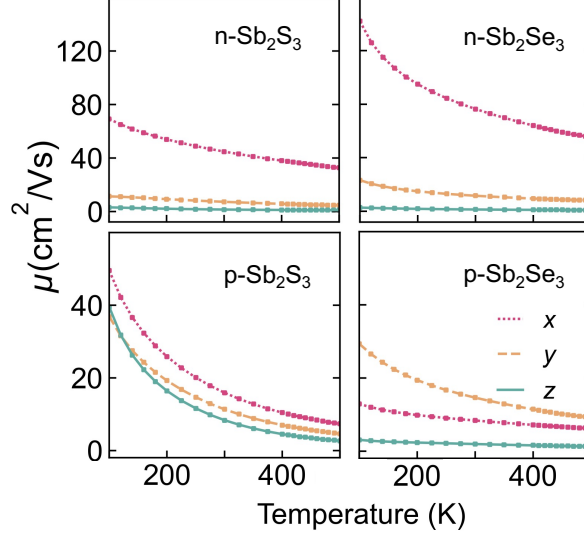


Figure 3: The anisotropic net carrier mobilities including all scattering mechanisms in Sb_2S_3 and Sb_2Se_3 as a function of temperature with a bulk defect concentration of 10^{17} cm^{-3} .

cal phonons (POP). Piezoelectric scattering was not considered due to the centrosymmetric crystal structure. The isotropically averaged mobilities are reasonably high at room temperature ($T = 300 \text{ K}$) for both electrons ($\sim 40 \text{ cm}^2 \text{ V}^{-1} \text{ s}^{-1}$) and holes ($\sim 15 \text{ cm}^2 \text{ V}^{-1} \text{ s}^{-1}$), at low and moderate defect concentrations ($< 1 \times 10^{18} \text{ cm}^{-3}$), indicating band-like transport (Fig. 2a). The hole mobilities are a little lower than the electron mobilities in both Sb_2S_3 and Sb_2Se_3 , suggesting that *n*-type doping could be beneficial for carrier collection in photovoltaic devices. This is in contrast to experimental measurements that have indicated higher mobility for *p*-type Sb_2Se_3 ,²⁶ however, this may be related to the doping asymmetry in these materials. The intrinsic mobility is limited by Fröhlich-type polar optical phonon scattering suggesting that large polarons are responsible for the transport behaviour (Fig. 2b). We note that large deformation potentials have been suggested as the origin of self-trapping in the bismuth double perovskites.⁵⁸ However, in Sb_2X_3 , acoustic deformation potential scattering is weak (due to small deformation potentials $< 6 \text{ eV}$), similar to that seen in the hybrid halide perovskites,^{59,60} indicating self-trapping is unlikely to occur via coupling with acoustic vibrations.

Table 2: Calculated mobilities of electrons (μ_e) and holes (μ_h) in Sb_2X_3 at 300 K under different defect concentrations (N_D) and experimental values for comparison. The anisotropy ratio (a_r) is defined as the ratio of maximum to minimum mobility

Material		Calculated ($\text{cm}^2 \text{V}^{-1} \text{s}^{-1}$)			Experiment ($\text{cm}^2 \text{V}^{-1} \text{s}^{-1}$)	
		N_D (cm^{-3})				
		10^{14}	10^{17}	10^{20}		
Sb_2S_3	μ_e	x	53.90	44.72	0.96	
		y	9.60	7.13	0.07	
		z	1.88	1.35	0.01	
		avg	21.79	17.73	0.35	
		a_r	28.67	33.13	96.00	
	μ_h	x	18.58	15.90	0.38	
		y	13.53	11.33	0.19	
		z	9.34	8.35	0.22	
		avg	13.82	11.86	0.26	6.4-12.8, ² 32.2-54.0 ²⁵
		a_r	1.99	1.90	2.00	
Sb_2Se_3	μ_e	x	89.97	76.38	1.96	
		y	16.74	11.65	0.11	
		z	1.94	1.41	0.01	
		avg	36.22	29.81	0.70	15 ²⁶
		a_r	46.38	54.17	196.00	
	μ_h	x	9.50	8.38	0.17	2.59 ⁵⁶
		y	16.95	14.63	0.25	1.17 ⁵⁶
		z	2.22	1.95	0.06	0.69 ⁵⁶
		avg	9.55	8.32	0.16	5.1, ²² 3.7-21.88, ²³ 45 ²⁶
		a_r	7.64	7.50	4.17	

The scattering from ionized impurities increases with the defect concentration. At concentrations around 10^{18}cm^{-3} , IMP and POP scattering are roughly the same strength and cause the mobility to reduce by a factor of a half (Fig. 2b). At higher defect concentrations transport is entirely dominated by ionized impurities. Our results indicate that careful control of defect concentrations are essential for preventing degradation of device efficiencies. This agrees well with previous experimental reports that the defect density is crucial to the carrier transport in Sb_2X_3 , whereby bulk defect densities above 10^{15}cm^{-3} led to significant degradation in conversion efficiency.⁶¹⁻⁶³ Furthermore, considering that most experimental mobility measurements in Sb_2X_3 were obtained from thin films where grain boundary scattering will further lower the mobility, we also tested the inclusion of mean free path scattering.

According to our results (Fig. S2 and Table S3), the mobilities in Sb_2X_3 are not significantly affected by grain boundary scattering even with grain sizes down to 10 nm, much smaller than the domain sizes typically seen in experiments.^{64–67} Accordingly, our results suggest that grain boundary scattering is unlikely to be a dominant source of scattering in Sb_2X_3 thin films, in agreement with previous studies.⁶⁸

The anisotropy of mobility was also considered. As shown in Table 2 and Fig. 3, our calculated mobilities are in reasonable agreement with the range of measured values. For electron transport, there is considerable anisotropy with the [100] direction showing roughly 6 times the mobility of the [010] direction and over 30 times the mobility of the [001] direction in both Sb_2S_3 and Sb_2Se_3 . For holes in Sb_2S_3 , there is a high mobility in the (001) plane where the transport is roughly isotropic and approximately twice that of the [001] direction. For holes in Sb_2Se_3 , the picture is slightly altered with the highest mobility seen along [010], roughly 2 times the mobility along [100] and 8 times the mobility along [001]. The anisotropy in mobility follows the anisotropy in the calculated effective masses and the Fermi-surface dimensionality.¹¹ Thus, as the electron mobilities are higher and more anisotropic than the hole mobilities, control of the grain orientation is necessary to achieve more efficient electronic transport in devices, which can be realised by strategies such as seed screening⁶⁹ and quasi-epitaxial growth.⁷⁰ Despite the anisotropic behaviour, even at moderate defect concentrations the electron and hole mobilities are still reasonably high ($>10 \text{ cm}^2 \text{ V}^{-1} \text{ s}^{-1}$) in at least two directions. The common description of Sb_2X_3 as a 1D semiconductors^{71,72} oversimplifies the nature of transport. Accordingly, it may be possible to obtain high mobility thin films, even when the grains are not fully aligned along the direction of the quasi-1D ribbons.

Conclusively, our results show no evidence for carrier self-trapping in Sb_2X_3 . While self-trapping has been proposed based on several experimental observations,^{15,73} large polaron carriers do not contradict these observations: i) a Stokes shift of 0.6 eV and broad photoluminescence (PL); ii) picosecond carrier decay kinetics; iii) absence of photoexcited carrier

density saturation (up to 10^{20} cm^{-3}); and iv) polarized light emission in Sb_2X_3 single crystals. Firstly, a large Stokes shift and broad PL is found in many chalcogenide semiconductors, especially those with deep defect levels such as Sb_2X_3 . Secondly, the timescale for carrier decay due to self-trapping is typically sub-picosecond or several picoseconds, while a timescale of tens of picoseconds is found in transient absorption (TA) measurements of Sb_2X_3 .^{15,73} We note that the understanding of TA kinetics in indirect band gap semiconductors is still evolving. Thirdly, the TA signal persists to high carrier densities (excitation power), which could also be explained by photoinduced absorption or a large trap density $> 10^{20} \text{ cm}^{-3}$.¹⁷ Finally, polarized light emission is found in many semiconductors and is connected to the crystal and defect structure. Therefore, we find no evidence that directly supports intrinsic carrier self-trapping in these materials.

In summary, we investigated the nature of charge carriers in Sb_2X_3 semiconductors. Our results strongly suggest that self-trapping (i.e. the formation of small polarons) is unlikely to occur and that instead charge transport involves large polarons with moderate mobility. In particular, we found: i) intermediate Fröhlich coupling constants (~ 2); ii) large Schultz polaron radii ($\sim 40 \text{ \AA}$); iii) the absence of electron or hole polaron formation in DFT calculations using the bond distortion and electron attractor methods; and iv) carrier mobilities $> 10 \text{ cm}^2 \text{ V}^{-1} \text{ s}^{-1}$ at room temperature for both electrons and holes (in agreement with experiments). We conclude that there is no theoretical evidence for small polaron formation in pristine Sb_2X_3 and self-trapping is unlikely to be the origin of the low open-circuit voltages in Sb_2X_3 devices as reported in previous studies.^{15,16} Accordingly, the low photovoltages may not be a bulk property of these materials and could be surmountable with improved fabrication and processing conditions to engineer the defect and interfacial properties of devices.

Methods

The Fröhlich polaron properties were solved using the open-source package POLARONMOBILITY.⁷⁴ The first-principles carrier scattering rates and resulting mobilities were calculated using AMSET.⁵⁷ The set of materials parameters used for these predictions are provided in Table S1–S2, S4–S6. The crystal structure was plotted using BLENDER⁷⁵ and BEAUTIFUL ATOMS.⁷⁶

All of the underlying electronic structure calculations were performed based on Kohn-Sham density-functional theory^{77,78} as implemented in Vienna Ab initio Simulation Package (VASP).⁷⁹ The projector augmented-wave (PAW) method⁸⁰ was employed with a plane-wave energy cutoff of 400 eV. All calculations were carried out using the Heyd-Scuseria-Ernzerhof hybrid functional (HSE06)^{81,82} with the D3 dispersion correction,⁸³ which have been proved to be able to well describe the structural and electronic properties in Sb_2X_3 .¹¹ The atomic positions were optimised until the Hellman-Feynman forces on each atom were below $0.0005 \text{ eV } \text{\AA}^{-1}$ for unit cells and $0.01 \text{ eV } \text{\AA}^{-1}$ for $3 \times 1 \times 1$ supercells. The energy convergence criterion was set to 10^{-6} eV . Γ -centered k -point meshes were set to $7 \times 2 \times 2$ and $2 \times 2 \times 2$ for geometry optimisation with primitive unit cells and supercells, respectively. For uniform band structure calculations which were used as inputs for AMSET, a denser k -point mesh of $19 \times 10 \times 10$ was used which is consistent with our previous calculations of carrier effective masses.¹¹ Detailed settings and convergence data are presented in Section S6 (Fig. S6 and Table S4–S6).

Acknowledgements

X.W. thanks Jarvist M. Frost, Yuchen Fu and Ye Yang for valuable discussions. We are grateful to the UK Materials and Molecular Modelling Hub for computational resources, which is partially funded by EPSRC (EP/P020194/1 and EP/T022213/1). X.W. acknowledges Imperial College London for a President’s PhD Scholarship. A.M.G. was supported by

EPSRC Fellowship EP/T033231/1. S.R.K. acknowledges the EPSRC Centre for Doctoral Training in the Advanced Characterisation of Materials (CDT-ACM)(EP/S023259/1) for a PhD studentship.

Supporting Information Available

Electronic band structures; formulas and input data of Fröhlich polaron coupling constant and Schultz polaron radius; effect of grain boundary scattering; workflow of localising a polaron; mobility parameters. Data produced during this work is freely available at: <https://dx.doi.org/10.17172/NOMAD/2022.08.11-2>.

Author Contributions

The author contributions have been defined following the CRediT system. X.W.: Conceptualization, Investigation, Formal analysis, Methodology, Visualization, Writing – original draft. A.M.G.: Methodology, Supervision, Writing – review & editing. S.R.K.: Methodology, Writing – review & editing. A.W.: Conceptualization, Methodology, Supervision, Writing – review & editing.

References

- (1) Versavel, M. Y.; Haber, J. A. Structural and optical properties of amorphous and crystalline antimony sulfide thin-films. *Thin Solid Films* **2007**, *515*, 7171–7176.
- (2) Liu, M.; Gong, Y.; Li, Z.; Dou, M.; Wang, F. A green and facile hydrothermal approach for the synthesis of high-quality semi-conducting Sb₂S₃ thin films. *Appl. Surf. Sci.* **2016**, *387*, 790–795.

- (3) Messina, S.; Nair, M.; Nair, P. Antimony selenide absorber thin films in all-chemically deposited solar cells. *J. Electrochem. Soc.* **2009**, *156*, H327.
- (4) Lai, Y.; Chen, Z.; Han, C.; Jiang, L.; Liu, F.; Li, J.; Liu, Y. Preparation and characterization of Sb_2Se_3 thin films by electrodeposition and annealing treatment. *Appl. Surf. Sci.* **2012**, *261*, 510–514.
- (5) Chen, C.; Li, W.; Zhou, Y.; Chen, C.; Luo, M.; Liu, X.; Zeng, K.; Yang, B.; Zhang, C.; Han, J., et al. Optical properties of amorphous and polycrystalline Sb_2Se_3 thin films prepared by thermal evaporation. *Appl. Phys. Lett.* **2015**, *107*, 043905.
- (6) Vadapoo, R.; Krishnan, S.; Yilmaz, H.; Marin, C. Self-standing nanoribbons of antimony selenide and antimony sulfide with well-defined size and band gap. *Nanotechnology* **2011**, *22*, 175705.
- (7) Vadapoo, R.; Krishnan, S.; Yilmaz, H.; Marin, C. Electronic structure of antimony selenide (Sb_2Se_3) from GW calculations. *Phys. Status Solidi B* **2011**, *248*, 700–705.
- (8) Nasr, T. B.; Maghraoui-Meherzi, H.; Abdallah, H. B.; Bennaceur, R. Electronic structure and optical properties of Sb_2S_3 crystal. *Physica B Condens. Matter.* **2011**, *406*, 287–292.
- (9) Savory, C. N.; Scanlon, D. O. The complex defect chemistry of antimony selenide. *J. Mater. Chem. A* **2019**, *7*, 10739–10744.
- (10) Lei, H.; Chen, J.; Tan, Z.; Fang, G. Review of recent progress in antimony chalcogenide-based solar cells: materials and devices. *Sol. RRL* **2019**, *3*, 1900026.
- (11) Wang, X.; Li, Z.; Kavanagh, S. R.; Ganose, A. M.; Walsh, A. Lone pair driven anisotropy in antimony chalcogenide semiconductors. *Phys. Chem. Chem. Phys.* **2022**, *24*, 7195–7202.

- (12) Choi, Y. C.; Lee, D. U.; Noh, J. H.; Kim, E. K.; Seok, S. I. Highly improved Sb_2S_3 sensitized-inorganic-organic heterojunction solar cells and quantification of traps by deep-level transient spectroscopy. *Adv. Funct. Mater.* **2014**, *24*, 3587–3592.
- (13) Duan, Z.; Liang, X.; Feng, Y.; Ma, H.; Liang, B.; Wang, Y.; Luo, S.; Wang, S.; Schropp, R. E.; Mai, Y., et al. Sb_2Se_3 thin film solar cells exceeding 10% power conversion efficiency enabled by injection vapor deposition (IVD) technology. *Adv. Mater.* **2022**, 2202969.
- (14) Green, M.; Dunlop, E.; Hohl-Ebinger, J.; Yoshita, M.; Kopidakis, N.; Hao, X. Solar cell efficiency tables (version 57). *Progress in photovoltaics: research and applications* **2021**, *29*, 3–15.
- (15) Yang, Z.; Wang, X.; Chen, Y.; Zheng, Z.; Chen, Z.; Xu, W.; Liu, W.; Yang, Y. M.; Zhao, J.; Chen, T., et al. Ultrafast self-trapping of photoexcited carriers sets the upper limit on antimony trisulfide photovoltaic devices. *Nat. Commun.* **2019**, *10*, 1–8.
- (16) Grad, L.; von Rohr, F. O.; Hengsberger, M.; Osterwalder, J. Charge carrier dynamics and self-trapping on Sb_2S_3 (100). *Phys. Rev. Mater.* **2021**, *5*, 075401.
- (17) Zhang, Z.; Hu, M.; Jia, T.; Du, J.; Chen, C.; Wang, C.; Liu, Z.; Shi, T.; Tang, J.; Leng, Y. Suppressing the trapping process by interfacial charge extraction in antimony selenide heterojunctions. *ACS Energy Lett.* **2021**, *6*, 1740–1748.
- (18) Grad, L.; von Rohr, F.; Zhao, J.; Hengsberger, M.; Osterwalder, J. Photoexcited charge carrier dynamics in Sb_2Se_3 (100). *Phys. Rev. Mater.* **2020**, *4*, 105404.
- (19) Chen, C.; Bobela, D. C.; Yang, Y.; Lu, S.; Zeng, K.; Ge, C.; Yang, B.; Gao, L.; Zhao, Y.; Beard, M. C., et al. Characterization of basic physical properties of Sb_2Se_3 and its relevance for photovoltaics. *Front. Optoelectron.* **2017**, *10*, 18–30.

- (20) Liu, H.; Luo, G.; Cheng, H.; Yang, Z.; Xie, Z.; Zhang, K. H.; Yang, Y. Ultrafast anisotropic evolution of photoconductivity in Sb_2Se_3 single crystals. *J. Phys. Chem. Lett.* **2022**, *13*, 4988–4994.
- (21) Ramo, D. M.; Shluger, A.; Gavartin, J.; Bersuker, G. Theoretical prediction of intrinsic self-trapping of electrons and holes in monoclinic HfO_2 . *Phys. Rev. Lett.* **2007**, *99*, 155504.
- (22) Zhou, Y.; Leng, M.; Xia, Z.; Zhong, J.; Song, H.; Liu, X.; Yang, B.; Zhang, J.; Chen, J.; Zhou, K., et al. Solution-processed antimony selenide heterojunction solar cells. *Adv. Energy Mater.* **2014**, *4*, 1301846.
- (23) Yuan, C.; Zhang, L.; Liu, W.; Zhu, C. Rapid thermal process to fabricate Sb_2Se_3 thin film for solar cell application. *Sol. Energy* **2016**, *137*, 256–260.
- (24) Li, J.; Huang, J.; Li, K.; Zeng, Y.; Zhang, Y.; Sun, K.; Yan, C.; Xue, C.; Chen, C.; Chen, T., et al. Defect-resolved effective majority carrier mobility in highly anisotropic antimony chalcogenide thin-film solar cells. *Sol. RRL* **2021**, *5*, 2000693.
- (25) Chalapathi, U.; Poornaprakash, B.; Park, S.-H. Influence of post-deposition annealing temperature on the growth of chemically deposited Sb_2S_3 thin films. *Superlattices Microstruct.* **2020**, *141*, 106500.
- (26) Black, J.; Conwell, E.; Seigle, L.; Spencer, C. Electrical and optical properties of some $\text{M}_2^{\text{V-B}}\text{N}_3^{\text{VI-B}}$ semiconductors. *J. Phys. Chem. Solids* **1957**, *2*, 240–251.
- (27) Yesugade, N.; Lokhande, C.; Bhosale, C. Structural and optical properties of electrodeposited Bi_2S_3 , Sb_2S_3 and As_2S_3 thin films. *Thin Solid Films* **1995**, *263*, 145–149.
- (28) El Zawawi, I.; Abdel-Moez, A.; Terra, F.; Mounir, M. Substrate temperature effect on the optical and electrical properties of antimony trisulfide thin films. *Thin Solid Films* **1998**, *324*, 300–304.

- (29) Torane, A.; Rajpure, K.; Bhosale, C. Preparation and characterization of electrodeposited Sb_2Se_3 thin films. *Mater. Chem. Phys.* **1999**, *61*, 219–222.
- (30) Caracas, R.; Gonze, X. First-principles study of the electronic properties of A_2B_3 minerals, with $\text{A} = \text{Bi}, \text{Sb}$ and $\text{B} = \text{S}, \text{Se}$. *Phys. Chem. Miner.* **2005**, *32*, 295–300.
- (31) Caruso, F.; Filip, M. R.; Giustino, F. Excitons in one-dimensional van der Waals materials: Sb_2S_3 nanoribbons. *Phys. Rev. B* **2015**, *92*, 125134.
- (32) Song, H.; Li, T.; Zhang, J.; Zhou, Y.; Luo, J.; Chen, C.; Yang, B.; Ge, C.; Wu, Y.; Tang, J. Highly anisotropic Sb_2Se_3 nanosheets: gentle exfoliation from the bulk precursors possessing 1D crystal structure. *Adv. Mater.* **2017**, *29*, 1700441.
- (33) Guo, L.; Zhang, B.; Qin, Y.; Li, D.; Li, L.; Qian, X.; Yan, F. Tunable quasi-one-dimensional ribbon enhanced light absorption in Sb_2Se_3 thin-film solar cells grown by close-space sublimation. *Sol. RRL* **2018**, *2*, 1800128.
- (34) Yang, W.; Ahn, J.; Oh, Y.; Tan, J.; Lee, H.; Park, J.; Kwon, H.-C.; Kim, J.; Jo, W.; Kim, J., et al. Adjusting the anisotropy of 1D Sb_2Se_3 nanostructures for highly efficient photoelectrochemical water splitting. *Adv. Energy Mater.* **2018**, *8*, 1702888.
- (35) Gusmão, R.; Sofer, Z.; Luxa, J.; Pumera, M. Antimony chalcogenide van der Waals nanostructures for energy conversion and storage. *ACS Sustain. Chem. Eng.* **2019**, *7*, 15790–15798.
- (36) Deringer, V. L.; Stoffel, R. P.; Wuttig, M.; Dronskowski, R. Vibrational properties and bonding nature of Sb_2Se_3 and their implications for chalcogenide materials. *Chem. Sci.* **2015**, *6*, 5255–5262.
- (37) Emin, D. *Polarons*; Cambridge University Press, 2013.
- (38) Fröhlich, H. Interaction of electrons with lattice vibrations. *Proc. Math. Phys. Eng.* **1952**, *215*, 291–298.

- (39) Stoneham, A. M. *Theory of defects in solids: electronic structure of defects in insulators and semiconductors*; Oxford University Press, 2001.
- (40) Schultz, T. Slow electrons in polar crystals: self-energy, mass, and mobility. *Phys. Rev.* **1959**, *116*, 526.
- (41) Parr, R. G., et al. W. Yang Density functional theory of atoms and molecules. *Oxford University Press* **1989**, *1*, 1989.
- (42) Pacchioni, G. Modeling doped and defective oxides in catalysis with density functional theory methods: Room for improvements. *The Journal of chemical physics* **2008**, *128*, 182505.
- (43) Pham, T. D.; Deskins, N. A. Efficient method for modeling polarons using electronic structure methods. *J. Chem. Theory Comput.* **2020**, *16*, 5264–5278.
- (44) Finazzi, E.; Di Valentin, C.; Pacchioni, G.; Selloni, A. Excess electron states in reduced bulk anatase TiO₂: comparison of standard GGA, GGA+U, and hybrid DFT calculations. *The Journal of chemical physics* **2008**, *129*, 154113.
- (45) Deák, P.; Aradi, B.; Frauenheim, T. Polaronic effects in TiO₂ calculated by the HSE06 hybrid functional: Dopant passivation by carrier self-trapping. *Phys. Rev. B* **2011**, *83*, 155207.
- (46) Di Valentin, C.; Pacchioni, G.; Selloni, A. Electronic structure of defect states in hydroxylated and reduced rutile TiO₂ (110) surfaces. *Phys. Rev. Lett.* **2006**, *97*, 166803.
- (47) Dudarev, S. L.; Botton, G. A.; Savrasov, S. Y.; Humphreys, C.; Sutton, A. P. Electron-energy-loss spectra and the structural stability of nickel oxide: An LSDA+U study. *Phys. Rev. B* **1998**, *57*, 1505.
- (48) Anisimov, V. I.; Aryasetiawan, F.; Lichtenstein, A. First-principles calculations of the

- electronic structure and spectra of strongly correlated systems: the LDA+U method. *J. Condens. Matter Phys.* **1997**, *9*, 767.
- (49) Deskins, N. A.; Rousseau, R.; Dupuis, M. Distribution of Ti^{3+} surface sites in reduced TiO_2 . *J. Phys. Chem. C* **2011**, *115*, 7562–7572.
- (50) Deskins, N. A.; Rousseau, R.; Dupuis, M. Localized electronic states from surface hydroxyls and polarons in TiO_2 (110). *J. Phys. Chem. C* **2009**, *113*, 14583–14586.
- (51) Shibuya, T.; Yasuoka, K.; Mirbt, S.; Sanyal, B. A systematic study of polarons due to oxygen vacancy formation at the rutile TiO_2 (110) surface by GGA+U and HSE06 methods. *J. Condens. Matter Phys.* **2012**, *24*, 435504.
- (52) Hao, X.; Wang, Z.; Schmid, M.; Diebold, U.; Franchini, C. Coexistence of trapped and free excess electrons in SrTiO_3 . *Phys. Rev. B* **2015**, *91*, 085204.
- (53) Liu, T.; Zhao, Q.; Li, C.; Lyu, Y.; Dupuis, M. Photocatalytic facet selectivity in BiVO_4 nanoparticles: Polaron electronic structure and thermodynamic stability considerations for photocatalysis. *J. Phys. Chem. C* **2019**, *123*, 20142–20151.
- (54) Lawal, A.; Shaari, A.; Ahmed, R.; Taura, L. Investigation of excitonic states effects on optoelectronic properties of Sb_2Se_3 crystal for broadband photo-detector by highly accurate first-principles approach. *Current Applied Physics* **2018**, *18*, 567–575.
- (55) Wang, K.; Chen, C.; Liao, H.; Wang, S.; Tang, J.; Beard, M. C.; Yang, Y. Both free and trapped carriers contribute to photocurrent of Sb_2Se_3 solar cells. *J. Phys. Chem. Lett.* **2019**, *10*, 4881–4887.
- (56) Chen, C.; Bobela, D. C.; Ye Yang,; Lu, S.; Zeng, K.; Ge, C.; Yang, B.; Gao, L.; Zhao, Y.; Beard, M. C.; Tang, J. Characterization of basic physical properties of Sb_2Se_3 and its relevance for photovoltaics. *Front. Optoelectron.* **2017**, *10*, 18–30.

- (57) Ganose, A. M.; Park, J.; Faghaninia, A.; Woods-Robinson, R.; Persson, K. A.; Jain, A. Efficient calculation of carrier scattering rates from first principles. *Nat. Commun.* **2021**, *12*, 1–9.
- (58) Wu, B.; Ning, W.; Xu, Q.; Manjappa, M.; Feng, M.; Ye, S.; Fu, J.; Lie, S.; Yin, T.; Wang, F., et al. Strong self-trapping by deformation potential limits photovoltaic performance in bismuth double perovskite. *Sci. Adv.* **2021**, *7*, eabd3160.
- (59) Wright, A. D.; Verdi, C.; Milot, R. L.; Eperon, G. E.; Pérez-Osorio, M. A.; Snaith, H. J.; Giustino, F.; Johnston, M. B.; Herz, L. M. Electron–phonon coupling in hybrid lead halide perovskites. *Nat. Commun.* **2016**, *7*, 1–9.
- (60) Lu, Y.-B.; Kong, X.; Chen, X.; Cooke, D. G.; Guo, H. Piezoelectric scattering limited mobility of hybrid organic-inorganic perovskites $\text{CH}_3\text{NH}_3\text{PbI}_3$. *Sci. Rep.* **2017**, *7*, 1–9.
- (61) Islam, M.; Thakur, A. Two stage modelling of solar photovoltaic cells based on Sb_2S_3 absorber with three distinct buffer combinations. *Sol. Energy* **2020**, *202*, 304–315.
- (62) Li, Z.-Q.; Ni, M.; Feng, X.-D. Simulation of the Sb_2Se_3 solar cell with a hole transport layer. *Mater. Res. Express* **2020**, *7*, 016416.
- (63) Khadir, A. Performance investigation of Sb_2S_3 and Sb_2Se_3 earth abundant based thin film solar cells. *Opt. Mater.* **2022**, *127*, 112281.
- (64) Rijal, S.; Li, D.-B.; Awni, R. A.; Bista, S. S.; Song, Z.; Yan, Y. Influence of post-selenization temperature on the performance of substrate-type Sb_2Se_3 solar cells. *ACS Appl. Energy Mater.* **2021**, *4*, 4313–4318.
- (65) Maghraoui-Meherzi, H.; Nasr, T. B.; Kamoun, N.; Dachraoui, M. Structural, morphology and optical properties of chemically deposited Sb_2S_3 thin films. *Physica B Condens. Matter.* **2010**, *405*, 3101–3105.

- (66) Perales, F.; Agullo-Rueda, F.; Lamela, J.; De las Heras, C. Optical and structural properties of $\text{Sb}_2\text{S}_3/\text{MgF}_2$ multilayers for laser applications. *J. Phys. D: Appl. Phys* **2008**, *41*, 045403.
- (67) Lokhande, C.; Sankapal, B.; Sartale, S.; Pathan, H.; Giersig, M.; Ganesan, V. A novel method for the deposition of nanocrystalline Bi_2Se_3 , Sb_2Se_3 and $\text{Bi}_2\text{Se}_3\text{--Sb}_2\text{Se}_3$ thin films—SILAR. *Appl. Surf. Sci.* **2001**, *182*, 413–417.
- (68) González, J. C.; Limborço, H.; Ribeiro-Andrade, R.; Silva, B. C.; Krambrock, K. Deciphering the role of defects in the ambipolar electrical transport in nanocrystalline Sb_2Se_3 thin films. *Adv. Electron. Mater.* **2022**, *8*, 2100985.
- (69) Li, K.; Chen, C.; Lu, S.; Wang, C.; Wang, S.; Lu, Y.; Tang, J. Orientation engineering in low-dimensional crystal-structural materials via seed screening. *Adv. Mater.* **2019**, *31*, 1903914.
- (70) Wang, L.; Li, D.-B.; Li, K.; Chen, C.; Deng, H.-X.; Gao, L.; Zhao, Y.; Jiang, F.; Li, L.; Huang, F., et al. Stable 6%-efficient Sb_2Se_3 solar cells with a ZnO buffer layer. *Nat. Energy* **2017**, *2*, 1–9.
- (71) Zhou, Y.; Wang, L.; Chen, S.; Qin, S.; Liu, X.; Chen, J.; Xue, D.-J.; Luo, M.; Cao, Y.; Cheng, Y., et al. Thin-film Sb_2Se_3 photovoltaics with oriented one-dimensional ribbons and benign grain boundaries. *Nat. Photonics* **2015**, *9*, 409–415.
- (72) Liang, X.; Guo, C.; Liu, T.; Liu, Y.; Yang, L.; Song, D.; Shen, K.; Schropp, R. E.; Li, Z.; Mai, Y. Crystallographic orientation control of 1D Sb_2Se_3 nanorod arrays for photovoltaic application by in situ back-contact engineering. *Sol. RRL* **2020**, *4*, 2000294.
- (73) Tao, W.; Zhu, L.; Li, K.; Chen, C.; Chen, Y.; Li, Y.; Li, X.; Tang, J.; Shang, H.; Zhu, H. Coupled electronic and anharmonic structural dynamics for carrier self-trapping in photovoltaic antimony chalcogenides. *Adv. Sci.* **2022**, 2202154.

- (74) Frost, J. M. Calculating polaron mobility in halide perovskites. *Phys. Rev. B* **2017**, *96*, 195202.
- (75) Community, B. O. Blender - a 3D modelling and rendering package. Blender Foundation: Stichting Blender Foundation, Amsterdam, 2018.
- (76) Wang, X.; Tian, T.; Ulrich, A. Beautiful Atoms: A python library for the manipulation and visualization of atomistic structure using blender. 2022; <https://github.com/beautiful-atoms/beautiful-atoms>, (accessed on 01/06/2022).
- (77) Kohn, W.; Sham, L. J. Self-consistent equations including exchange and correlation effects. *Phys. Rev.* **1965**, *140*, A1133.
- (78) Dreizler, R. M.; Gross, E. K. *Density Functional Theory*; Springer, 1990; pp 245–271.
- (79) Kresse, G.; Furthmüller, J. Efficient iterative schemes for ab initio total-energy calculations using a plane-wave basis set. *Phys. Rev. B* **1996**, *54*, 11169.
- (80) Kresse, G.; Joubert, D. From ultrasoft pseudopotentials to the projector augmented-wave method. *Phys. Rev. B* **1999**, *59*, 1758.
- (81) Heyd, J.; Scuseria, G. E.; Ernzerhof, M. Hybrid functionals based on a screened Coulomb potential. *J. Chem. Phys.* **2003**, *118*, 8207–8215.
- (82) Krukau, A. V.; Vydrov, O. A.; Izmaylov, A. F.; Scuseria, G. E. Influence of the exchange screening parameter on the performance of screened hybrid functionals. *J. Chem. Phys.* **2006**, *125*, 224106.
- (83) Grimme, S. Accurate description of van der Waals complexes by density functional theory including empirical corrections. *J. Comput. Chem.* **2004**, *25*, 1463–1473.

Supporting Information

Band Versus Polaron: Charge Transport in Antimony Chalcogenides

Xinwei Wang,[†] Alex M. Ganose,[†] Seán R. Kavanagh,^{†,‡} and Aron Walsh^{*,†}

[†] *Department of Materials, Imperial College London, Exhibition Road, London SW7 2AZ, UK*

[‡] *Thomas Young Centre and Department of Chemistry, University College London, 20 Gordon Street, London WC1H 0AJ, UK*

E-mail: a.walsh@imperial.ac.uk

S1. Electronic band structures

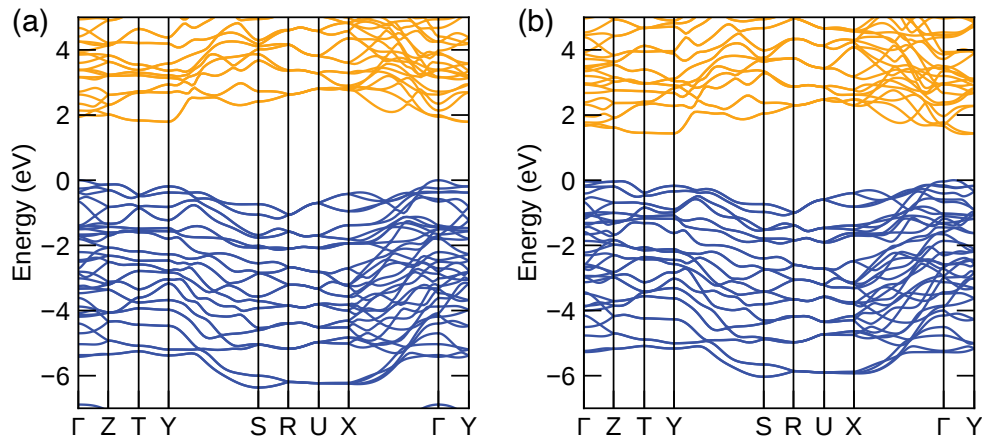


Figure 1: Electronic band structures of (a) Sb_2S_3 and (b) Sb_2Se_3 .

S2. Fröhlich polaron coupling constant and Schultz polaron radius

Table 1: Parameters used to calculate Fröhlich polaron coupling constant α . The effective phonon frequency (ω) is in THz

Material		ϵ_∞	ϵ_0	ω	m^*	
					e	h
Sb ₂ S ₃	avg	10.26	68.76	3.49	0.40	0.64
	<i>x</i>				0.16	0.47
	<i>y</i>				0.92	0.65
	<i>z</i>				5	0.97
Sb ₂ Se ₃	avg	13.52	76.27	2.57	0.35	0.90
	<i>x</i>				0.14	0.85
	<i>y</i>				0.81	0.55
	<i>z</i>				7	3

The long-range electron-longitudinal optical phonon coupling can be expressed by the dimensionless Fröhlich polaron coupling constant α ¹

$$\alpha = \frac{e^2}{\hbar} \left(\frac{1}{\epsilon_\infty} - \frac{1}{\epsilon_0} \right) \sqrt{\frac{m^*}{2\hbar\omega}}, \quad (1)$$

where ϵ_∞ and ϵ_0 are the high-frequency and static dielectric constants, respectively, m^* is the effective mass and ω is the effective phonon frequency. The effective mass and effective frequency were calculated using the AMSET package.² The isotropic α was obtained using the harmonic mean of the effective masses and the arithmetic average of the dielectric constants. The anisotropic α was calculated using the anisotropic (direction-dependent) effective masses, consistent with previous work.³

Table 2: Parameters used to calculate Schultz polaron radius (r_f , Å)

Material		α		v		w		m_P^*	
		e^-	h^+	e^-	h^+	e^-	h^+	e^-	h^+
Sb_2S_3	avg	1.6	2.0	12.70	12.98	11.16	10.99	0.52	0.89
	x	1.0	1.8	12.34	12.79	11.39	11.11	0.19	0.62
	y	2.4	2.1	13.25	12.99	10.82	10.98	1.38	0.91
	z	5.7	2.5	16.07	13.30	9.32	10.79	14.88	1.47
Sb_2Se_3	avg	1.3	2.1	16.72	17.29	15.32	14.96	0.42	1.20
	x	0.8	2.0	16.40	17.24	15.53	14.99	0.16	1.12
	y	2.0	1.6	17.21	16.95	15.01	15.17	1.06	0.69
	z	5.8	3.8	20.68	18.68	13.05	14.12	17.59	5.25

Schultz polaron radius is defined as⁴

$$r_f = \sqrt{\frac{3}{2\mu v}}, \quad (2)$$

$$\mu = \frac{v^2 - w^2}{v^2}, \quad (3)$$

where v and w are Feynman-model variational parameters which specify the polaron state. They are solved variationally by the Feynman polaron model using Fröhlich polaron coupling constant α as an input. μ is the reduced effective mass.

S3. Effect of grain boundary scattering

Table 3: Calculated mobilities of electrons (μ_e) and holes (μ_h) in Sb_2X_3 at 300 K with and without grain boundary scattering. The anisotropy ratio (a_r) is defined as the ratio of maximum to minimum mobility

Material	Calculated mobility ($\text{cm}^2 \text{V}^{-1} \text{s}^{-1}$)				
		Mean free path (nm)			
		-	100	10	
Sb_2S_3	μ_e	x	44.72	43.98	38.57
		y	7.13	7.07	6.55
		z	1.35	1.34	1.25
		avg	17.73	17.46	15.45
		a_r	33.13	32.82	30.86
	μ_h	x	15.90	15.77	14.71
		y	11.33	11.25	10.58
		z	8.35	8.29	7.82
		avg	11.86	11.77	11.04
		a_r	1.90	1.90	1.88
Sb_2Se_3	μ_e	x	76.38	74.56	62.14
		y	11.65	11.46	10.07
		z	1.41	1.39	1.23
		avg	29.81	29.13	24.48
		a_r	54.17	53.64	50.52
	μ_h	x	8.38	8.29	7.57
		y	14.63	14.41	12.78
		z	1.95	1.93	1.81
		avg	8.32	8.21	7.38
		a_r	7.50	7.47	7.06

The effect of grain boundary scattering on the mobility in Sb_2X_3 was evaluated by incorporating an average grain size using the AMSET package.² The grain boundary scattering lifetime is set to v_g/L , where v_g is the group velocity and L is the mean free path. In this work, the mean free path of 10 and 100 nm were tested. The carrier concentration and defect concentration were assumed to be 10^{13}cm^{-3} and 10^{17}cm^{-3} , respectively.

According to our results (Table 3 and Fig. 2), at temperatures between 100 and 500 K, the total mobility is not limited by the grain boundary scattering. The anisotropic values at room temperature are shown in Table 3. After considering the grain boundary scattering,

the values of anisotropy ratio change slightly and the most favourable directions for carrier transport remain the same for both Sb_2S_3 and Sb_2Se_3 .

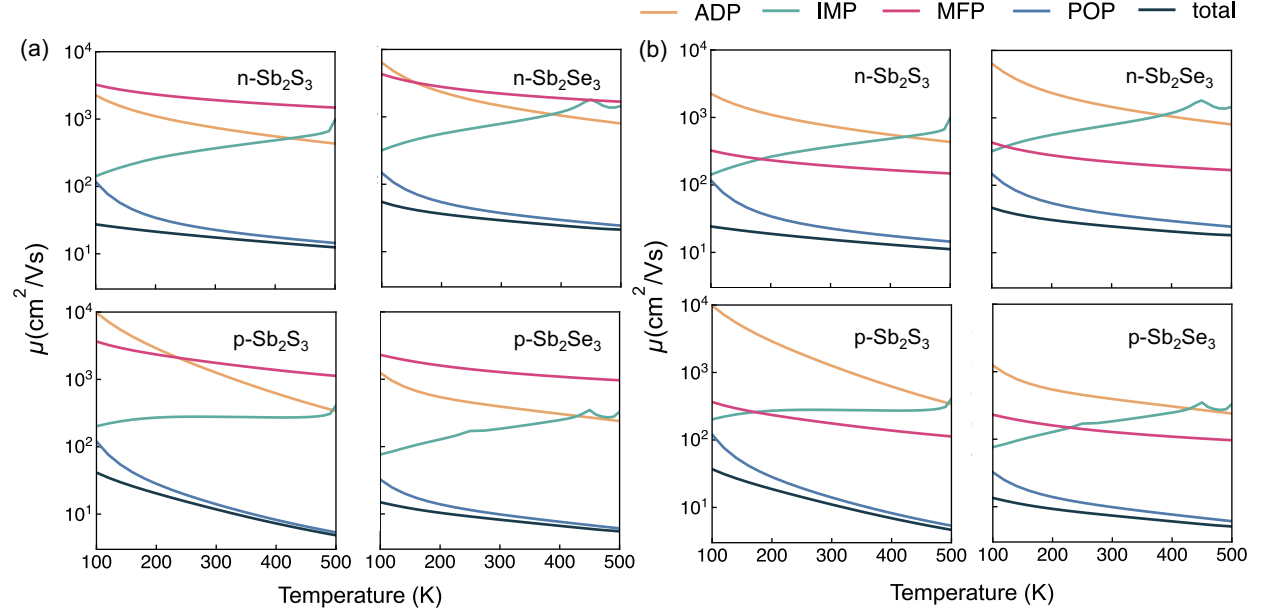


Figure 2: Calculated component and total mobilities with mean free path of (a) 100 nm and (b) 10 nm as a function of temperature.

S4. Workflow of localising a polaron in Sb_2X_3

We attempted to localise an electron or a hole in Sb_2S_3 and Sb_2Se_3 by the bond distortion method and electron attractor method (Fig. 3). A $3 \times 1 \times 1$ supercell (with the dimension of $11.40 \times 11.20 \times 11.39 \text{ \AA}^3$ and $11.85 \times 11.55 \times 11.93 \text{ \AA}^3$ for Sb_2S_3 and Sb_2Se_3 , respectively) was constructed, which is sufficient to model small polarons.⁵⁻⁷ In each system, one electron per supercell was added or removed to introduce an electron or a hole.

We first applied the bond distortion method to introduce distortions around one designated atom (Sb for adding an electron and S/Se for adding a hole) for each non-equivalent Sb and S/Se. These are implemented by the ShakeNBreak package.^{8,9} Different distortions of 20%, 30% and 40% with both compression and stretching were considered. However, after structural optimisation, all lowest-energy structures relaxed to perfect configurations.

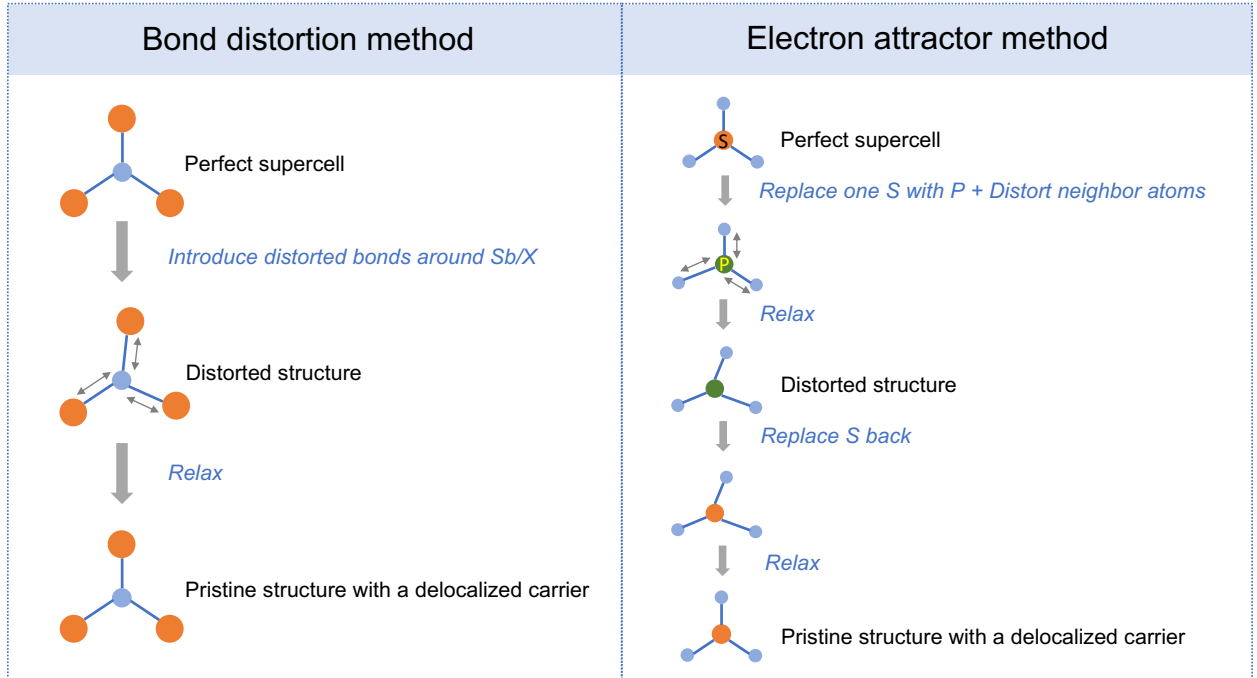


Figure 3: The workflow of bond distortion method and electron attractor method.

We further combined the bond distortion method with the electron attractor method to confirm the formation of hole polarons in Sb_2S_3 . The electron attractor method refers to attracting electrons or holes to a particular atomic site by replacing one certain atom. Phosphorous has stronger attraction to holes than sulfur as it contains fewer protons and has a lower electronegativity. Here, we used one P to replace one S in a supercell, introduced some local distortions around the P atom and add small random displacements to all atoms to break the symmetry in the initial structures. Three non-equivalent S sites were considered, and a range of distortions of both compression and stretching between 0% and 60% with 10% as an interval were tested. The number of electrons were kept the same as the neutral replaced system, suggesting one extra hole in Sb_2S_3 . The structures with the substituted atom and local distortions were fully relaxed. Finally, for each non-equivalent S case, we used the lowest-energy structures among different distortions, replaced back the S atom and relaxed the configuration again. Nevertheless, all structures went back to perfect configurations, indicating that the localised polarons are unlikely to form.

Nevertheless, we note that using a k -point mesh of $1\times 1\times 1$ to do geometry relaxation could lead to localised solution in some cases (Fig. 4a). While after converging it with denser k -point mesh of $2\times 2\times 2$, we finally get delocalised polarons (Fig. 4b).

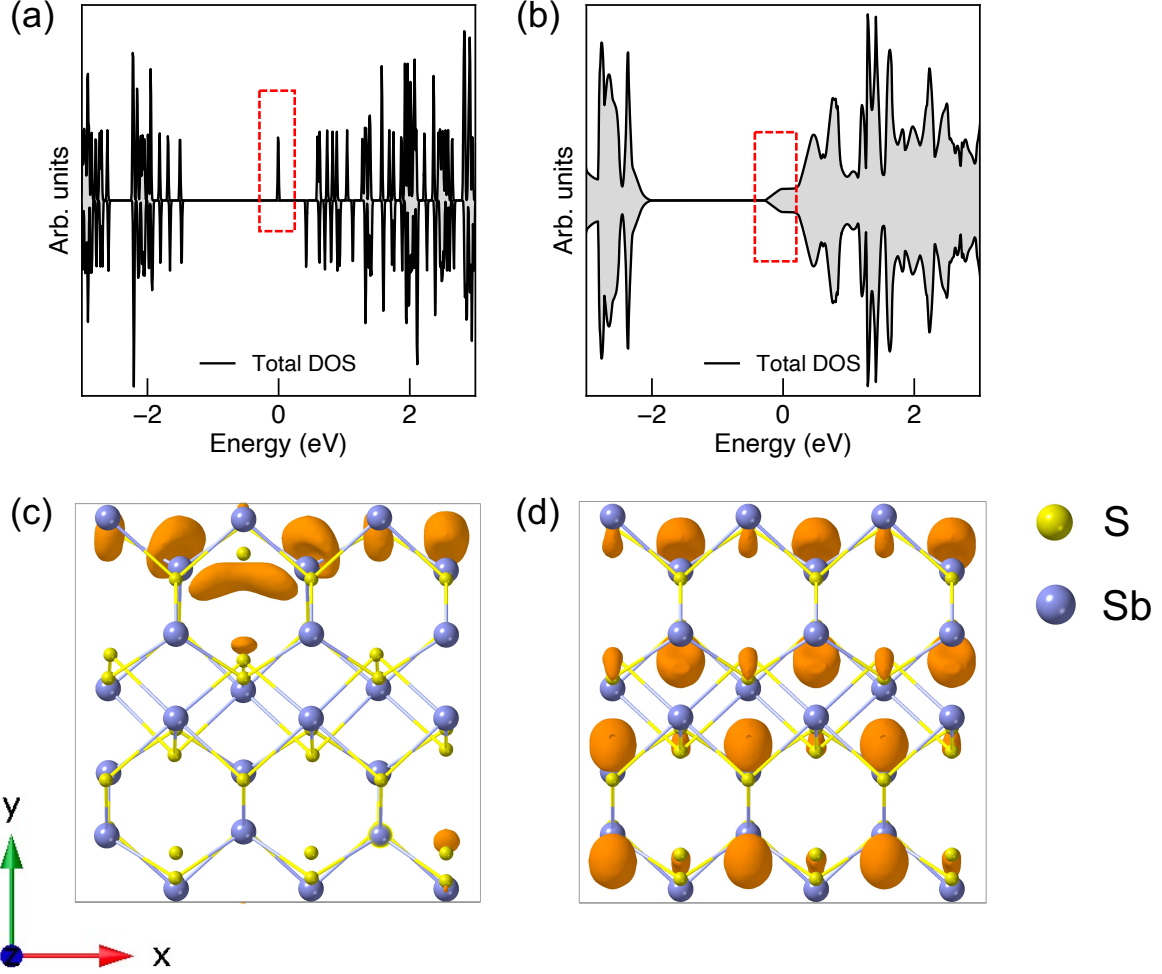


Figure 4: (a-b) Density of states and (c-d) partial charge densities of conduction band maximum for electron polarons in Sb_2S_3 using a k -point mesh of (a) and (c) $1 \times 1 \times 1$, (b) and (d) $2 \times 2 \times 2$ to relax structures. The partial charge densities were plotted by specifying the energy range of the conduction band maxima, which are represented by red dashed rectangles. The isosurface value for partial charge densities is set to $0.01 \text{ e}/\text{\AA}^3$.

S5. Partial charge densities of electron and hole polarons

Partial charge densities of the valence band maximum (VBM) for hole polarons and conduction band maximum (CBM) for electron polarons in Sb_2X_3 are shown in Fig. 5, which are delocalised in all cases.

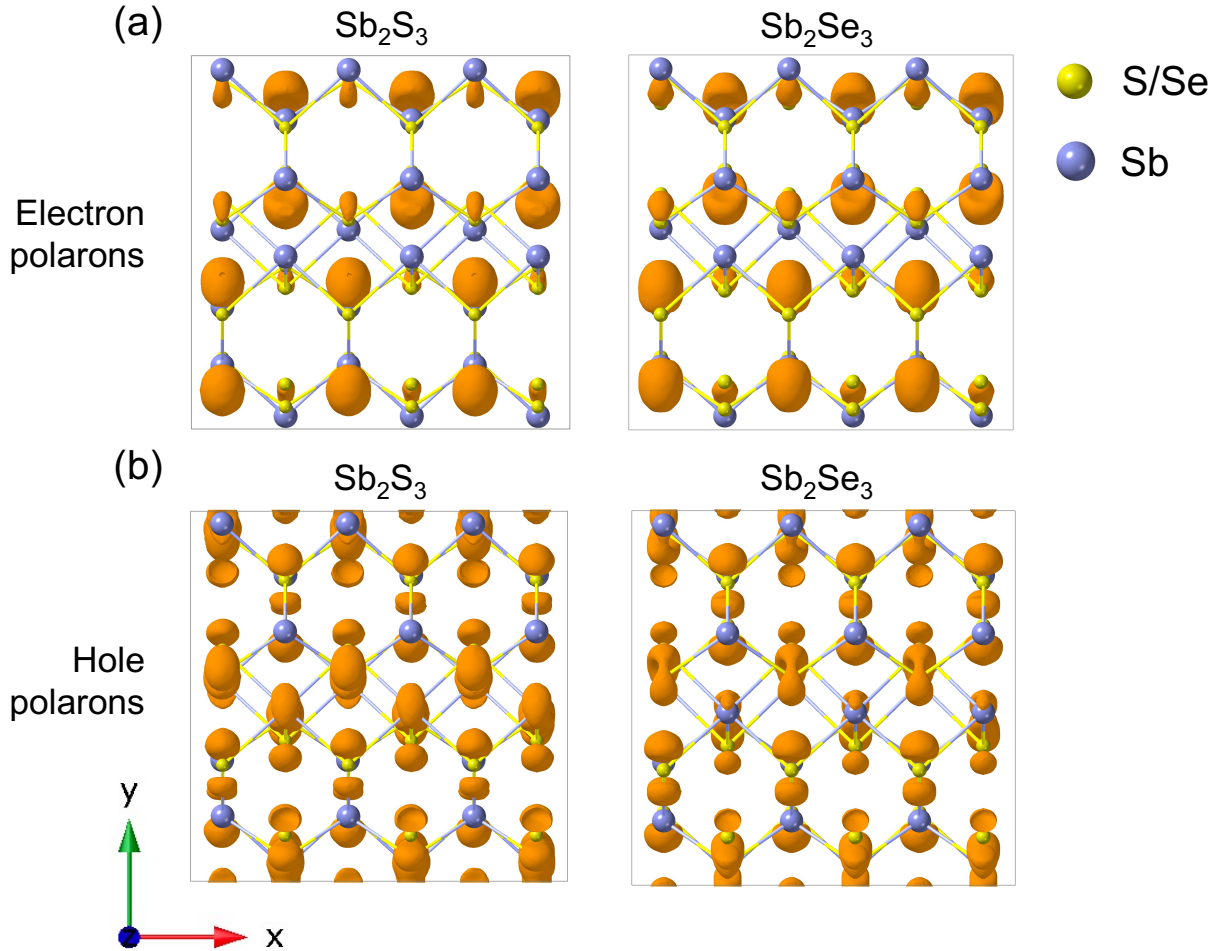


Figure 5: Partial charge densities of (a) conduction band maximum for electron polarons and (b) valence band maximum for hole polarons in Sb_2S_3 and Sb_2Se_3 . The isosurface values for partial charge densities are set to 0.01 and 0.005 $e/\text{\AA}^3$ for electron and hole polarons, respectively.

S6. Parameters used to calculate mobilities in Sb_2X_3

The k -point meshes used to calculate transport properties were tested (shown in Fig. 6) and a k -point mesh of $169 \times 57 \times 57$ is used for all calculations. The carrier concentration was set to 10^{13} cm^{-3} according to previous experimental results in Sb_2X_3 .^{10–16} The calculated effective phonon frequency is 3.49 for Sb_2S_3 and 2.57 for Sb_2Se_3 . The calculated deformation potentials, elastic constants and dielectric constants are shown in Table 4, 5 and 6, respectively.

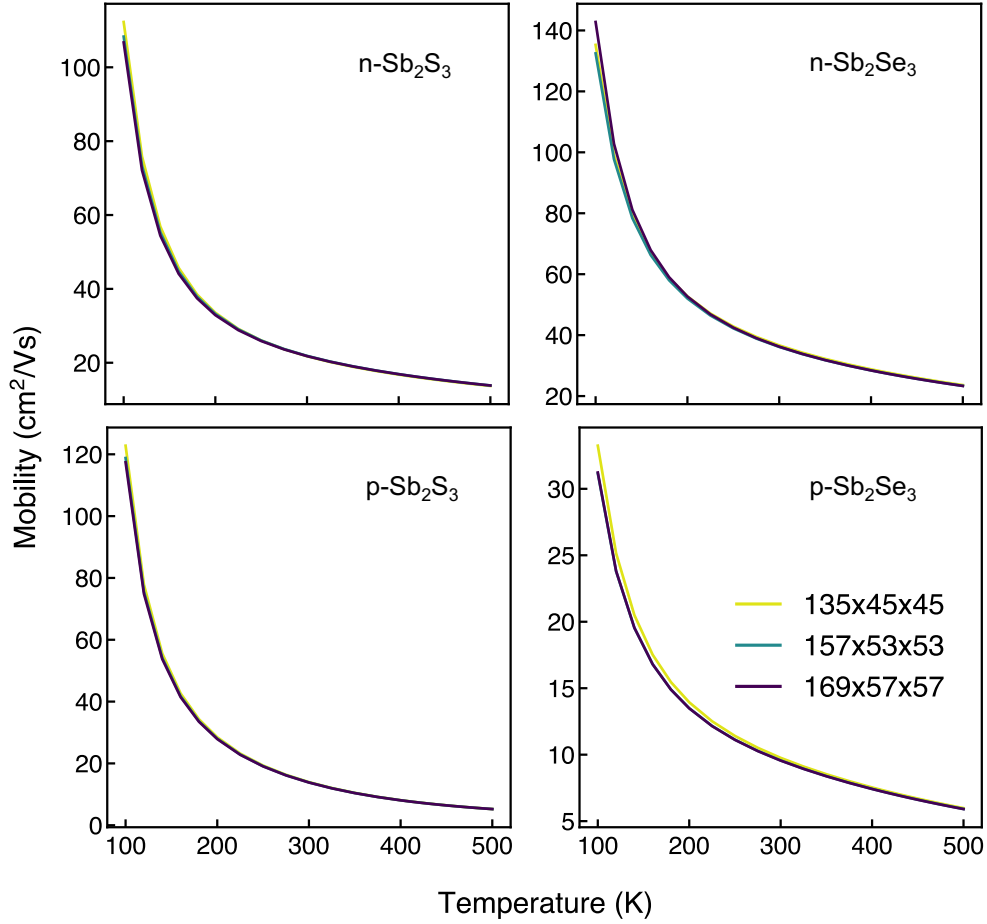


Figure 6: The convergence of mobility in Sb_2X_3 under different k -point meshes. The defect concentration is set to be 10^{14} cm^{-3} and the temperature is set to be 300 K.

Table 4: Calculated deformation potentials (D, eV) for the upper valence and lower conduction bands of Sb_2S_3 and Sb_2Se_3

Material			D_{XX}	D_{YY}	D_{ZZ}
Sb_2S_3	VBM	D_{XX}	5.41	0.26	0.07
		D_{YY}	0.26	0.10	0.02
		D_{ZZ}	0.07	0.02	1.27
	CBM	D_{XX}	5.26	0.42	0.17
		D_{YY}	0.42	2.43	3.35
		D_{ZZ}	0.17	3.35	2.62
Sb_2Se_3	VBM	D_{XX}	0.53	0.16	0.05
		D_{YY}	0.16	2.86	0.03
		D_{ZZ}	0.05	0.03	2.47
	CBM	D_{XX}	3.31	0.36	0.09
		D_{YY}	0.36	0.39	0.29
		D_{ZZ}	0.09	0.29	1.38

Table 5: Calculated elastic constants (in GPa) of Sb_2S_3 and Sb_2Se_3

Material		C_{XX}	C_{YY}	C_{ZZ}	C_{XY}	C_{YZ}	C_{ZX}
Sb_2S_3	C_{XX}	93.75	28.00	18.50	0.00	0.00	0.00
	C_{YY}	28.00	57.25	15.39	0.00	0.00	0.00
	C_{ZZ}	18.50	15.39	37.69	0.00	0.00	0.00
	C_{XY}	0.00	0.00	0.00	31.68	0.00	0.00
	C_{YZ}	0.00	0.00	0.00	0.00	17.11	0.00
	C_{ZX}	0.00	0.00	0.00	0.00	0.00	8.77
Sb_2Se_3	C_{XX}	77.15	25.63	17.11	0.00	0.00	0.00
	C_{YY}	25.63	54.15	17.03	0.00	0.00	0.00
	C_{ZZ}	17.11	17.03	31.75	0.00	0.00	0.00
	C_{XY}	0.00	0.00	0.00	23.42	0.00	0.00
	C_{YZ}	0.00	0.00	0.00	0.00	18.41	0.00
	C_{ZX}	0.00	0.00	0.00	0.00	0.00	5.08

Table 6: Calculated static (ϵ_0) and high-frequency (ϵ_∞) dielectric constants of Sb_2S_3 and Sb_2Se_3

Material	ϵ_0			ϵ_∞		
	x	y	z	x	y	z
Sb_2S_3	98.94	94.21	13.14	11.55	10.97	8.25
Sb_2Se_3	85.64	128.18	15.00	15.11	14.92	10.53

References

- (1) Fröhlich, H. Interaction of electrons with lattice vibrations. *Proc. Math. Phys. Eng.* **1952**, *215*, 291–298.
- (2) Ganose, A. M.; Park, J.; Faghaninia, A.; Woods-Robinson, R.; Persson, K. A.; Jain, A. Efficient calculation of carrier scattering rates from first principles. *Nat. Commun.* **2021**, *12*, 1–9.
- (3) Guster, B.; Melo, P.; Martin, B. A.; Brousseau-Couture, V.; de Abreu, J. C.; Miglio, A.; Giantomassi, M.; Côté, M.; Frost, J. M.; Verstraete, M. J., et al. Fröhlich polaron effective mass and localization length in cubic materials: degenerate and anisotropic electronic bands. *Phys. Rev. B* **2021**, *104*, 235123.
- (4) Schultz, T. Slow electrons in polar crystals: self-energy, mass, and mobility. *Phys. Rev.* **1959**, *116*, 526.
- (5) Sun, L.; Huang, X.; Wang, L.; Janotti, A. Disentangling the role of small polarons and oxygen vacancies in CeO₂. *Phys. Rev. B* **2017**, *95*, 245101.
- (6) Ding, H.; Lin, H.; Sadigh, B.; Zhou, F.; Ozolins, V.; Asta, M. Computational investigation of electron small polarons in α -MoO₃. *J. Phys. Chem. C* **2014**, *118*, 15565–15572.
- (7) Castleton, C. W.; Lee, A.; Kullgren, J. Benchmarking density functional theory functionals for polarons in oxides: Properties of CeO₂. *J. Phys. Chem. C* **2019**, *123*, 5164–5175.
- (8) Mosquera-Lois, I.; Kavanagh, S. R. In search of hidden defects. *Matter* **2021**, *4*, 2602–2605.
- (9) Mosquera-Lois, I.; Kavanagh, S. R.; Walsh, A.; Scanlon, D. O. Identifying the ground state structures of point defects in solids. *arXiv preprint arXiv:2207.09862* **2022**, (accessed on 25/07/2022).

- (10) Chen, C.; Bobela, D. C.; Yang, Y.; Lu, S.; Zeng, K.; Ge, C.; Yang, B.; Gao, L.; Zhao, Y.; Beard, M. C., et al. Characterization of basic physical properties of Sb_2Se_3 and its relevance for photovoltaics. *Front. Optoelectron.* **2017**, *10*, 18–30.
- (11) Liu, M.; Gong, Y.; Li, Z.; Dou, M.; Wang, F. A green and facile hydrothermal approach for the synthesis of high-quality semi-conducting Sb_2S_3 thin films. *Appl. Surf. Sci.* **2016**, *387*, 790–795.
- (12) Zhou, Y.; Leng, M.; Xia, Z.; Zhong, J.; Song, H.; Liu, X.; Yang, B.; Zhang, J.; Chen, J.; Zhou, K., et al. Solution-processed antimony selenide heterojunction solar cells. *Adv. Energy Mater.* **2014**, *4*, 1301846.
- (13) Yuan, C.; Zhang, L.; Liu, W.; Zhu, C. Rapid thermal process to fabricate Sb_2Se_3 thin film for solar cell application. *Sol. Energy* **2016**, *137*, 256–260.
- (14) Li, J.; Huang, J.; Li, K.; Zeng, Y.; Zhang, Y.; Sun, K.; Yan, C.; Xue, C.; Chen, C.; Chen, T., et al. Defect-resolved effective majority carrier mobility in highly anisotropic antimony chalcogenide thin-film solar cells. *Sol. RRL* **2021**, *5*, 2000693.
- (15) Chalapathi, U.; Poornaprakash, B.; Park, S.-H. Influence of post-deposition annealing temperature on the growth of chemically deposited Sb_2S_3 thin films. *Superlattices Microstruct.* **2020**, *141*, 106500.
- (16) Black, J.; Conwell, E.; Seigle, L.; Spencer, C. Electrical and optical properties of some $\text{M}_2^{\text{V-B}}\text{N}_3^{\text{VI-B}}$ semiconductors. *J. Phys. Chem. Solids* **1957**, *2*, 240–251.